

A novel approach to detect line emission under high background in high-resolution X-ray spectra

Xiangyu Zhang^{1*}, Sara Algeri¹, Vinay Kashyap², and Margarita Karovska²,

¹*School of Statistics, University of Minnesota, Minneapolis, MN, 55455, USA*

²*Center for Astrophysics | Harvard & Smithsonian, 60 Garden St., Cambridge, MA 02138, USA*

Accepted 2023 February 1. Received 2023 February 1; in original form 2022 December 3

ABSTRACT

We develop a novel statistical approach to identify emission features or set upper limits in high-resolution spectra in the presence of high background. The method relies on detecting differences from the background using smooth tests and using classical likelihood ratio tests to characterise known shapes like emission lines. We perform signal detection or place upper limits on line fluxes while accounting for the problem of multiple comparisons. We illustrate the method by applying it to a *Chandra* LETGS+HRC-S observation of symbiotic star RT Cru, successfully detecting previously known features like the Fe line emission in the 6-7 keV range and the Iridium-edge due to the mirror coating on *Chandra*. We search for thermal emission lines from Ne X, Fe XVII, O VIII, and O VII, but do not detect them, and place upper limits on their intensities consistent with a ≈ 1 keV plasma. We serendipitously detect a line at 16.93 Å that we attribute to photoionisation or a reflection component.

Key words: binaries: symbiotic – methods: data analysis – methods: statistical

1 INTRODUCTION

Recently, several new X-ray missions and mission concepts have been developed with the goal of obtaining high-resolution spectra (e.g., XRISM [XRISM Science Team 2022; Ishisaki et al. 2022], Athena [Barret et al. 2022], Arcus [Smith 2020], LEM [Kraft et al. 2022]). With such spectra expected to become a ubiquitous feature of high-energy investigations, it is necessary to consider the challenge of detecting weak features when the spectrum is also contaminated by high levels of background of both instrumental and cosmic origins. Traditional methods employed for spectral analysis, like globally fitting simplified spectral models, or carrying out isolated analyses of individual spectral lines, will fail to produce robust results; the former when the data show more structure than is encoded in the models, and the latter when statistical fluctuations in the background confound the detection of weak features.

Here, we present a newly developed statistical approach to evaluate the significance of deviations that may be present in high-resolution spectra even in the presence of high background (Algeri 2020, 2021). The method works by comparing a postulated model for the background and a source-free background dataset, to assess the validity of the former and, if needed, provide a data-driven correction for it based on the information carried by the latter. Once the background model has been “trained” on the signal-free sample, our strategy is to employ *smooth tests*, originally introduced by Neyman (1937), to assess whether the source spectrum of interest shows any *shape* differences from the re-calibrated background model. Whenever significant deviations cannot be found, we then search for the presence of the most prominent spectral lines at well-defined loca-

tions by means of likelihood ratio tests and place strict upper limits on their fluxes following the framework of Kashyap et al. (2010). The statistical properties of the procedure proposed, i.e., power and probability of type I error, are also investigated.

Our method is applicable to high-resolution spectra, i.e., one where the resolution of the detector is sufficient to separate individual emission lines. In the case of low-resolution spectra, the presence or absence of individual lines must be inferred by modeling (see, e.g., Park et al. 2008). In this setting, Bayesian solutions are often implemented in order to overcome the difficulties associated with low bin counts and the lack of model identifiability within the digitization limits of the spectra. In contrast, here we implement an *unbinned* analysis on data obtained as lists of photons. The goal is to detect differences between the likelihoods under the background-only and the background+source hypotheses.

Estimation and inference can then be facilitated by conducting a separate analysis over different regions of the spectrum following a frequentist statistical paradigm. The inferential results are ultimately combined by implementing adequate corrections for multiple hypothesis testing.

To illustrate the necessity of the method proposed here in the analysis of high-resolution spectra, we apply it to study the symbiotic stellar system RT Cru through the analysis of the *Chandra* LETGS+HRC-S dataset. We emphasize that the method itself has been developed to have general applicability to high-energy high-resolution datasets where weak spectral features are expected over strong background contamination. We describe the RT Cru system and the *Chandra* data below in Section 2.1, and demonstrate the need for a principled statistical method to obtain robust inferences. We then provide a detailed description of *smooth models* and *smooth tests* in Section 3. In Section 4, we describe the analysis that we carry

* zhan6004@umn.edu

out. Specifically, in Section 4.1 we focus on the implementation of data-driven background correction, in Section 4.2 we implement the proposed testing procedure to detect spectral features, and in Section 4.3 we construct upper limits for specified line locations where no signal is detected. The applicability of the method and the results of the analysis are discussed in Section 5. We summarise our work in Section 6.

2 THE RELEVANCE OF RT Cru

In order to demonstrate the suitability of smooth tests in detecting new signals when the data is contaminated by high background, we apply it to answer questions that arose during the analysis of *Chandra* spectra of RT Cru, and which could not be dealt with using existing methods. Below, we describe the astronomical object, and the dataset, and illustrate how an improved statistical analysis is necessary.

RT Cru is a symbiotic system (distance 2.5 kpc; GAIA EDR3) where a high-mass white dwarf (WD; $M_{WD} > 1.3 M_{\odot}$) accretes from the wind of an M5 III red giant companion (Cieslinski et al. 1994). Symbiotic systems have been invoked as potential progenitors of a fraction of SN type Ia - key cosmological indicators. Symbiotic systems, especially those containing a high-mass ($> 1.3 M_{\odot}$) white dwarf component are important for understanding the possibility of a single degenerate path toward SN Ia.

Symbiotic systems produce soft X-ray spectra from the accretion disk surrounding the WD, through quasi-steady burning of the accreting material on the WD surface (Muerse et al. 1997), and from a jet.

A handful of systems have also been detected in hard X-rays, including RT Cru (INTEGRAL, Bird et al. 2007; *Swift*, Kennea et al. 2009; *Suzaku*, Ducci et al. 2016, *Chandra*, Luna & Sokolowski 2007; Danehkar et al. 2021; *NuSTAR+Suzaku+Swift*, Luna et al. 2018). The nature of the hard X-ray emission is not well-established, though it is thought to be attributable to the presence of an accretion disk: the hard X-rays have been variously modeled as isobaric cooling flows (Luna & Sokolowski 2007); or partially covered (Kennea et al. 2009) or clumpy absorption of thermal emission (Danehkar et al. 2021); or post-shock regions above the polar caps of a magnetized white dwarf (Ducci et al. 2016), and are able to explain the features of the spectrum at high energies ($E \gtrsim 3$ keV).

RT Cru also exhibits several variability features like aperiodic flickering at timescales of a few ks, and a strong correlation of spectral hardness with overall brightness, with higher intensities corresponding to softer spectra (see Danehkar et al. 2021). Such features are characteristic of emission driven by changes near the inner boundary of the accretion disk. The question that arises then is what the origin of this variability could be. As noted above, the observed X-ray spectrum has been variously modeled as an intrinsic change in the soft thermal emission component as well as changes in a continuum component due to intervening absorption. The presence of spectral lines during increases of soft flux, especially if they are the dominant contributors to the soft emission, would support the former scenario, while the lack of such lines would favor the latter scenario. The *Chandra*/LETGS+HRC-S data we focus on below (Section 2.1) was originally obtained to settle this question, but the analysis was limited because of the relatively high background encountered. While an adequate spectral fit that included partial covering of a thermal component was obtained by Danehkar et al. (2021), the fit was driven by the higher energy signal. Thus, the nature of the soft emission remained unsettled.

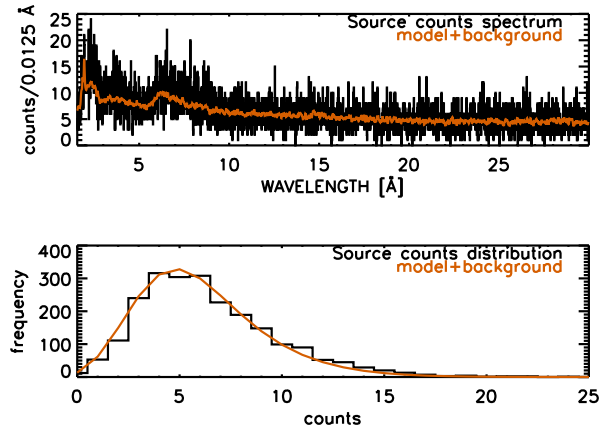


Figure 1. Comparing the spectrum of RT Cru with the model from Danehkar et al. (2021). *Top:* The *Chandra*/LETGS+HRC-S counts spectrum is shown as the black histogram, and the sum of the estimated background and the predicted model are shown in red. *Bottom:* The distribution of counts in each bin in the observed spectrum is shown as the black histogram, and the expected Poisson distribution based on the model intensity and the estimated background is shown as the red curve.

2.1 Data collection: the *Chandra*/LETGS+HRC-S Observation

RT Cru has been observed extensively with both *Swift*/*XRT* and the *Chandra* gratings. Here we focus specifically on the *Chandra*/LETGS+HRC-S observations that were carried out in Nov 2015 for a total of 78.9 ks (PI: M. Karovska; ObsIDs 16688 and 17810) and whose analysis was described by Danehkar et al. (2021). Danehkar et al. modeled the spectrum as a combination of a power-law component (with index $\Gamma \approx 1.7$), a thermal soft excess (with temperature ≈ 1.3 keV), and an ad hoc triplet of emission lines from Fe $K\alpha$, Fe XXV, and Fe XXVI in the 6-7 keV region. The observed spectrum is shown in the top panel of Figure 1 in the $\lambda = [1.56, 30]$ Å wavelength range (corresponding to photon energies $E = [0.41, 8]$ keV) as the black histogram, along with the best-fit astrophysical model spectrum (together with the estimated background contribution) as the red curve. The hard emission in the 6-7 keV range likely originates close to the accretor, e.g., from a region of the boundary layer of the accretion disk or a bright spot. It could also be associated with collisional excitation in the vicinity of the WD accretor, including in the inner-jet regions (e.g., Kennea et al. 2009, Karovska et al. 2010, Eze 2014).

However, the soft component of this model is not well constrained, partly due to the lack of sensitivity of *Swift* and *Chandra*/ACIS detectors at $E \lesssim 2$ keV and the high instrument background present in *Chandra*/LETGS+HRC-S. The advantage of high spectral resolution observations is that emission lines, if they exist, can be located, and their presence and identification can provide useful diagnostic information about the emitting plasma. The high background in the LETGS+HRC-S spectrum makes this a difficult problem. The upper panel of Figure 1 shows several spikes that could be tagged as spectral lines, but the question arises as to how significant each of those identifications would be. Methods that are typically used in these situations compare the heights of the spikes to the baseline intensity levels, and flag them as significant if they exceed a certain threshold. But the large number of bins present in high-resolution spectra implies that the chances of false positives being flagged as a line are high. This is demonstrated in the bottom panel of Fig-

Passbands of interest (W_r)	Passband range		Dominant lines and Features		N_r	n_r
	[Å]	[keV]	[Å]			
W_1	1.65-2.05	6.05-7.5	Fe K	1.785/1.853/1.944	6879	368
W_2	5.5-10.2	1.2-2.25	Ir-M edge	≈ 6.5	75699	3311
W_3	11.5-13.0	0.95-1.08	Ne X	12.131	22809	730
W_4	14.6-15.15	0.82-0.85	Fe XVII	15.014	8354	247
W_5	16.2-17.4	0.71-0.765	Fe XVII	17.051	17331	471
W_6	18.5-19.5	0.65-0.67	O VIII	18.967	14060	390
W_7	21.3-21.75	0.57-0.582	O VII(r)	21.602	6192	179
W_8	21.65-22.0	0.564-0.573	O VII(i)	21.804	4927	145
W_9	21.9-23.0	0.539-0.566	O VII(f)	22.101	15255	390

Table 1. Summary of wavelength bands of interest. The second column of the table reports the wavelength range (in Å) of each of the regions, W_r , $r = 1, \dots, 9$, considered. The expected spectral lines and their expected positions (in Å) on each of the regions are listed in the third and fourth columns. The size of the source-free sample (N_r) and the physics sample (n_r) for each of the region r are given in the last two columns.

ure 1, which compares the observed distribution of counts in the bins (black stepped histogram) with the expected Poisson distribution derived from the model and background (smooth red curve). Typically, a threshold is set based on the expected distribution such that a tolerable number of false detections are accepted; this tolerance can be set as accepting one false detection over the sample (as is done in, e.g., `wavdetect`; Freeman et al. 2002). There are ≈ 2280 bins in the observed spectrum shown in the upper panel, yielding $p < 0.000044$ as the required threshold value (note that the usual "3 σ " detection criterion often used in astronomy corresponds to $p < 0.0027$, and adopting it would result in as many as 6 false claims of detection; this issue will worsen when higher resolution spectra covering larger wavelength ranges are obtained), which translates to the requirement that a fluctuation exceeds 20 counts before it can be considered significant.

The goal of this observation was to obtain a spectrum at wavelengths $\lambda \gtrsim 6$ Å (energies $E \lesssim 2$ keV), where the sensitivity of the instrument is higher on average than previous observations, in particular at the locations dominated by Ne X $\lambda 12.13$ and the two Fe XVII lines at $\lambda\lambda 15.01, 17.05$. In addition, we also consider other wavelength ranges like the Fe K region (where spectral lines have indeed been detected and modeled) and wavelength regions where O VIII $\lambda 18.96$ and the O VII He-like triplets at $\lambda\lambda 21.6, 21.8, 22.1$ are to be found. These wavelength bands of interest are denoted with W_r , $r = 1, \dots, 9$ and are listed in Table 1; the Table shows the wavelength range, the dominant structure expected in these bands, and the number of events within the passbands in both the source region (n_r) as well as the source-free background region (N_r (collected in an area $39.4\times$ greater than the source region)). The observed spectra (black histograms) and model predicted spectra (green curves) are shown, along with the expected background (red curves), zoomed in to these wavelength regions in Figure 2; the expected locations of spectral lines of interest are marked with yellow shaded regions centered around vertical green lines.

Inspection of the spectral regions of interest in Figure 2 shows hints that some emission structure may be present in some cases, e.g., in passbands W_3 (Ne X), W_5 (Fe XVII), W_6 (O VIII), W_7 (O VII(r)), and W_8 (O VII(i)). We carry out a naive estimation of the line intensities by counting the number of photons within ± 0.1 Å (corresponding to the width of the line response) at the putative locations of the lines, collected within both the source and background datasets, and computing the Bayesian posterior density of the line intensities (viz. Primini & Kashyap 2014). Table 2 lists the mode and the 68% highest posterior density (HPD) intervals for the resulting posterior distributions for each line or band of interest. Several line intensities are estimated formally at significance $> 1\sigma$. An

Wavelength Band	Model ^a Expected	Estimate ^b Observed
W_1	175.7	186 $^{<205}_{>167}$
W_2	1021.0	1370 $^{<1430}_{>1310}$
12.131 ± 0.1 Å $\subset W_3$	16.4	20.0 $^{>10.9}_{>31.2}$
15.014 ± 0.1 Å $\subset W_4$	12.7	20.6 $^{>11.4}_{>15.2}$
17.051 ± 0.1 Å $\subset W_5$	9.15	5.6 $^{>1.4}_{>26.3}$
18.967 ± 0.1 Å $\subset W_6$	6.78	16.1 $^{>6.7}_{>0}$
21.602 ± 0.1 Å $\subset W_7$	2.8	0 $^{>0}_{>19.5}$
21.804 ± 0.1 Å $\subset W_8$	2.6	9.8 $^{>3.5}_{>4.8}$
22.101 ± 0.1 Å $\subset W_9$	2.5	0 $^{>0}_{>0}$

a: Expected model counts based on Danehkar et al. (2021)

b: Mode of the posterior density distribution of source intensity (Primini & Kashyap 2014) and the 68% HPD (highest posterior density) uncertainty bounds

Table 2. Model predicted and estimated counts at line locations of interest.

analysis that ignores the problem of multiple tests would claim detections of these lines, but it is possible that such claims would turn out to be false positives. A more careful and principled method must be used to evaluate their reality. We, therefore, employ the method proposed in (Algeri 2020, 2021) to adequately model background shapes on each of the regions considered. Moreover, since our analysis requires us to test for the presence of one or more lines on each of the above-mentioned regions, adequate corrections for multiple hypotheses testing are also implemented. Such step is necessary to ensure that the overall probability of a false discovery across any of the regions considered does not exceed the desired significance level. Finally, we also test whether the feature present at 16.93 Å in W_5 , shortward of the Fe XVII $\lambda 17.04$ line by ≈ 2100 km s⁻¹ is real, in the sense of being detectable.

We find that none of the hypothesised thermal spectral lines listed in Table 2 are detectable (see Section 4.2.2), and thus we place upper limits on the strengths of the lines that are well above reasonable variations in the fitted spectral model (cf. expected model counts listed in Table 2). In contrast, we find that the serendipitously identified line at 16.93 Å is detectable with a corrected p -value ≈ 0.01 . We discuss the possible origins of this line in Section 5.

3 STATISTICAL METHODS

As outlined in Sections 1-2, the presence of high background makes it necessary to adequately characterise its shape and discern its characteristic features from random fluctuations. We show here that this can be done by means of *smooth models* and *smooth tests* originally introduced in statistical literature by Neyman (1937).

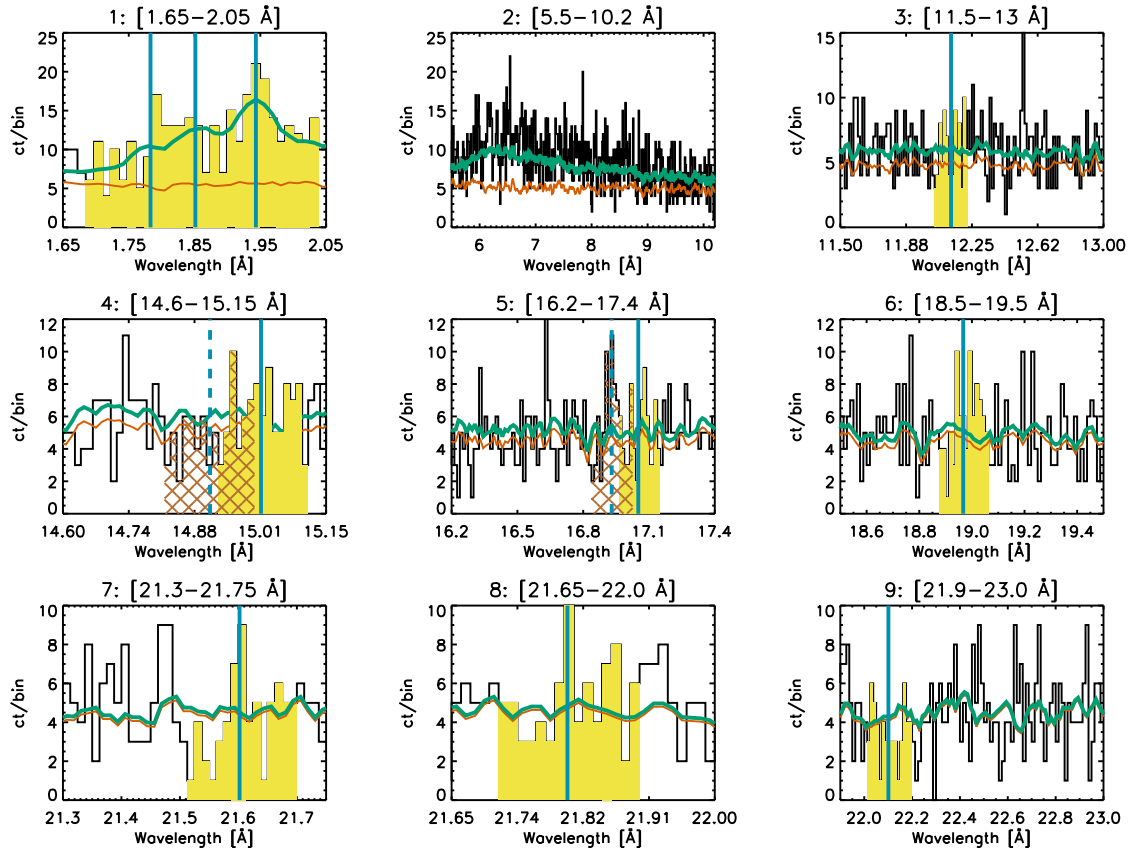


Figure 2. The counts spectrum of RT Cru (Figure 1), without background subtraction, zoomed in to the various bands of interest (see Table 1). The counts spectrum is shown as the black histogram, with the best-fit model spectrum from [Danehkar et al. \(2021\)](#) shown as the green curve. The estimated smoothed background is shown as the red curve. The blue vertical lines indicate the lines of interest in each band (except for W_2 , which covers an instrument feature). The shaded yellow regions cover the approximate widths of the line response for each of the lines studied here. The brown cross-hatched regions in passbands W_4 and W_5 mark serendipitous testing locations (see Discussion).

In the context of the analysis of high-resolution spectra, smooth tests are particularly useful in that they naturally integrate estimation and inference to adequately handle uncertain background shapes. Moreover, when aiming to detect new signals, they provide a trade-off between tests of hypotheses and goodness-of-fit tests. Specifically, while tests of hypotheses, such as the Likelihood Ratio Test (LRT) (e.g., [Wilks 1938](#)), are known to have high power towards a well-specified alternative model, their validity is severely undermined if the models under comparison are misspecified. In our case, this would occur, for instance, when searching for a few strong spectral line at the wrong position, or when the deviations from the background are due to the signal of a continuous, widely spread source. A classical approach to obviate this problem is that of relying on classical goodness-of-fit tests, such as Kolmogorov-Smirnov ([Kolmogorov 1933](#); [Smirnov 1939](#)), or Pearson’s χ^2 ([Pearson 1900](#)), and which are expected to have some power against all possible deviations from the background model. However, since different tests have higher power towards different alternatives, they may not be sensible in detecting deviations towards the desired direction. Smooth tests, on the other hand, enjoy high power only towards a finite number of possible directions. Interestingly, the user can rely on suitable data-driven procedures to select the most “significant” directions towards which deviations from the background occur. Therefore, they effectively let the data decide “where to look”.

From a methodological perspective, the scope of our analysis is three folds. Our first goal is to assess the validity of our postulated

background model and, when needed, provide a data-driven correction for it. Second, we aim to determine whether the Chandra LETGS+HRC-S Data provides significant evidence to conclude that spectral lines are present in addition to the background. Third, in regions where no significant deviations from the background model are detected, we proceed by setting upper limits on the intensity of the expected signals. In order to achieve these goals, we rely on suitably constructed *smooth tests* and likelihood-ratio tests.

3.1 Smooth Models and Smooth Tests

Smooth tests are an inferential procedure for model assessment originally introduced by [Neyman \(1937\)](#). In the context of astronomical spectra, they are particularly advantageous because, in addition to validating the postulated astrophysical models, they also provide valuable insights on how misspecified models can be improved by means of smooth models. The latter consist of an “updated” version of the initial proposed model on the basis of the data observed. Sections 3.1-3.3 outline the main steps characterising these procedures.

3.1.1 Data-driven Model Calibration via Smooth Models

Let X be a continuous random variable with an unknown cumulative distribution function (CDF) F , and an unknown probability density function (PDF) f . F corresponds to the true distribution from

Table 3. Summary of the notation used throughout the manuscript.

Symbol	Definition
Section 3.1:	
X	Random variable with unknown distribution F
x	The value of X observed on the data
F	Unknown cumulative distribution function (cdf) of X
f	Unknown probability density function (pdf) of X
G	Hypothesised cdf of X
g	Hypothesised pdf of X
$d(u; G, F)$	ratio between the densities f and g evaluated at $u = G(x)$
$\{h_j(u)\}_{j \geq 0}$	A series of orthonormal basis functions on $[0, 1]$
θ_j	j^{th} coefficient of the orthonormal expansion for $d(u; G, F)$
$\hat{\theta}_j$	Estimate of θ_j
m	Number of terms used in the expansion for $d(u; G, F)$
$\hat{d}(u; G, F)$	Estimate of $d(u; G, F)$
\hat{f}	Smooth estimator of f
D_m	Deviance statistic
d_m	The value of D_m observed on the data
K_m	K-statistic
k_m	The value of K_m observed on the data
α	A pre-specified significance level
Section 3.2:	
M	Upper bound for the selection of m
$\hat{\theta}_{(j)}$	The j^{th} largest (in magnitude) among the coefficients θ_j
Section 3.3:	
$D_{(m)}$	Post-selection Deviance statistic
$d_{(m)}$	The value of $D_{(m)}$ observed on the data
$K_{(m)}$	Post-selection K-statistic
$k_{(m)}$	The value of $K_{(m)}$ observed on the data
Section 4.1:	
W_r	r^{th} wavelength band of interest, $r = 1, \dots, 9$
B_{W_r}	True unknown background distribution for region W_r
b_{W_r}	True unknown background density for region W_r
g_{W_r}	Postulated uniform background density for region W_r
\hat{B}_{W_r}	Corrected background distribution for region W_r
\hat{b}_{W_r}	Corrected background density for region W_r
C_w	w^{th} calibration region, $w = 1, \dots, 5$
\hat{b}_{C_w}	Corrected background density for combined region C_w
N_r	The size of the source-free sample for the region r
n_r	The size of the physics sample for the region r
Section 4.2:	
F_r	Unknown distribution for physics sample for region W_r
f_r	Unknown density for physics sample for region W_r
Section 4.3:	
s_r	Density of spectral line for region W_r , $r = 3, \dots, 9$
η_r	Relative intensity of the expected signal for region W_r
q_r	Density of physics sample for region W_r

which our data were generated. Despite F being unknown, we aim to assess if it can be reasonably approximated by a hypothesised distribution G , with PDF g . The goal is to test the hypotheses

$$H_0 : F = G; \quad \text{vs} \quad H_1 : F \neq G \quad (1)$$

To perform the test in (1), we begin by rewriting the true density, f , as a function of the postulated model g , i.e.,

$$f(x) = g(x)d(G(x); G, F) \quad (2)$$

where $d(G(x); G, F) = \frac{f(x)}{g(x)}$; that is, $d(G(x); G, F)$ corresponds to the density ratio between f and g and can be expressed in the quantile domain as

$$d(u; G, F) = \frac{f(G^{-1}(u))}{g(G^{-1}(u))} \quad \text{with } u = G(x) \in [0, 1]$$

where $G^{-1}(u)$ is the quantile function of X under model G . In statistics literature, $d(u; G, F)$ is also referred to as "comparison density" (e.g. Parzen 2004); such nomenclature is used to emphasise that $d(u; G, F)$ is the PDF of the random variable $U = G(X)$ (see proposition 3.1 in Algeri 2021).

Under the assumption that the density $d(u; G, F)$ is square integrable on the unit interval, we can represent it via a series of orthonormal basis functions $\{h_j(u)\}_{j \geq 0}$, i.e.,

$$d(u; G, F) = 1 + \sum_{j=1}^{\infty} \theta_j h_j(u) \quad (3)$$

with $h_0(u) = 1$ and $\theta_j = \int_0^1 h_j(u) d(u; G, F) du$. The choice of the basis functions h_j in (3) is arbitrary. For example, in virtue of their simple implementation and generalisability to the discrete setting, a popular choice are the normalised shifted Legendre polynomials (e.g., Neyman 1937; Ledwina 1994).

A *smooth model* can then be specified by truncating the series in (3) at a point m . Moreover, once a set of independent and identically distributed observations, x_1, \dots, x_n , has been collected, the coefficients θ_j are estimated via

$$\hat{\theta}_j = \frac{1}{n} \sum_{i=1}^n h_j(G(x_i)) = \frac{1}{n} \sum_{i=1}^n h_j(u_i). \quad (4)$$

It follows that an estimator of $d(G(x); G, F)$ in (3) is

$$\hat{d}(G(x); G, F) = 1 + \sum_{j=1}^m \hat{\theta}_j h_j(G(x)). \quad (5)$$

Finally, a *smooth estimator* of the true density f is

$$\hat{f}(x) = g(x) \hat{d}(G(x); G, F) = g(x) \left[1 + \sum_{j=1}^m \hat{\theta}_j h_j(G(x)) \right]. \quad (6)$$

As described in Section 3.1.2, this modeling strategy naturally leads to the inferential framework needed to test the hypotheses in (1).

3.1.2 Smooth Tests

We begin by considering the simplified scenario where the point of truncation, m , in (5) is fixed and all the first m coefficients are included in our estimators in (5) and (6). This simplifying assumption allows us to introduce the main asymptotic results at the core of our inferential strategy. A detailed discussion on model selection and adequate inferential adjustments is postponed to Sections 3.2-3.3.

The decomposition in (2) allows us to rewrite the hypotheses in (1) as

$$\begin{aligned} H_0 : d(u; G, F) &= 1 \quad \text{for all } u \in [0, 1], \quad \text{versus} \\ H_1 : d(u; G, F) &\neq 1 \quad \text{for some } u \in [0, 1] \end{aligned} \quad (7)$$

Furthermore, by exploiting our estimator in (5), we can reformulate (7) as

$$\begin{aligned} H_0 : \theta_1 = \dots = \theta_m &= 0 \quad \text{versus} \\ H_1 : \theta_j &\neq 0 \quad \text{for at least one } j = 1, \dots, m \end{aligned} \quad (8)$$

Notice that H_0 in (7) implies H_0 in (8) but H_1 in (7) does not imply H_1 in (8). Whereas, H_1 in (8) implies H_1 in (7) and thus by testing H_0 and H_1 in (8) we can determine if the true distribution F deviates significantly from our hypothesised distribution G .

To test the hypotheses in (8), we rely on two different test statistics. A common choice in the context of smooth tests (e.g. Ledwina

1994; Kallenberg & Ledwina 1997) is the deviance statistic, i.e.,

$$D_m = n \sum_{j=1}^m \hat{\theta}_j^2; \quad (9)$$

whereas, in this manuscript, we propose, in addition to (9), the use of the *K*-statistic which specifies as

$$K_m = \max_{j=1, \dots, m} n \hat{\theta}_j^2.$$

It is easy to show (e.g. Algeri 2020) that, under H_0 , and as $n \rightarrow \infty$, the estimators $\hat{\theta}_j$ in (4) converge in distribution to normally distributed random variable with mean zero and variance $1/n$. It follows that

$$D_m = \sum_{j=1}^m (\sqrt{n} \hat{\theta}_j)^2 \xrightarrow{d} \chi_m^2.$$

Hence, an asymptotic p-value for the deviance test is

$$\text{p-value} = P(\chi_m^2 > d_m) \quad (10)$$

where d_m is the value of D_m observed on the data.

The asymptotic distribution of the K-statistic under H_0 can be derived by noticing that, asymptotically, K_m is distributed as the maximum of m χ_1^2 distributed random variables. Therefore, letting k_m be the observed value of K_m on the data, its asymptotic p-value is

$$\text{p-value} = 1 - P(\chi_1^2 \leq k_m)^m. \quad (11)$$

The respective proof can be found in Appendix A.

The null hypothesis is rejected when the p-value is smaller than a pre-specified significance level α . For example, a discovery claim at 2σ significance corresponds to a level α of approximately 0.05. A rejection of the null hypothesis implies the postulated model g deviates significantly from the true model f .

3.2 Model Selection

An important step of our analysis is that of selecting the basis functions to be included in our estimators (5) and (6). Here, we rely on a model selection process based on the Bayesian information criterion (BIC) for selection (e.g., Algeri 2021), and can be summarised as follows:

- i. Choose a suitably large value M (usually 10).
- ii. Obtain the estimates $\hat{\theta}_1, \dots, \hat{\theta}_M$ as in (4).
- iii. Rearrange $\hat{\theta}_j^2$ in decreasing order, i.e.,

$$\hat{\theta}_{(1)}^2 \geq \hat{\theta}_{(2)}^2 \geq \dots \geq \hat{\theta}_{(M)}^2,$$

with $\hat{\theta}_{(j)}^2$ denoting the j th largest squared coefficient.

- iv. Choose the largest m that maximises

$$\text{BIC}(m) = \sum_{j=1}^m \hat{\theta}_{(j)}^2 - \frac{m \log n}{n}. \quad (12)$$

The procedure outlined here is data-dependent, that is, the value of m selected may vary over different samples. It is therefore necessary to account for the randomness associated with the model selection process. This can be done as described in Section 3.3.

3.3 Post-selection Inference Adjustments

Traditional inference is typically constructed under the assumption that the model under study has been selected independently

from the data available. In many practical scenarios, however, a data-driven selection procedure is typically implemented, and thus, classical inferential results fail to hold due to the randomness associated with the selection process. While one can easily overcome this problem by relying on data splitting (e.g. Moran 1973; Cox 1975), or bootstrapping (e.g. Algeri & Zhang 2021), in our setting, it is possible to identify suitable post-selection adjustments for the p-values in (10) and (11).

For what concerns the deviance statistic, a post-selection adjusted p-value can be constructed as described in Algeri (2021). Specifically, let

$$D_{(m)} = \sum_{j=1}^m \hat{\theta}_{(j)}^2$$

be the deviance statistic obtained as the sum of the squares of the m largest estimated coefficients, with m selected via the BIC criterion in (12), and denote with $d_{(m)}$ be its value observed on the data. An adjusted p-value for the test in (8) is

$$\text{p-value}_{adj, \mathcal{M}} = P(\chi_M^2 > d_{(m)}). \quad (13)$$

Notice that, conversely from (10), in (13) the observed value of the deviance statistic is compared to a χ_M^2 rather than χ_m^2 . In virtue of its conservativeness, we refer to the correction in (13) as "naive correction".

An alternative approach consists of applying the usual Bonferroni's correction (e.g. Miller 1977) and typically used in the context of multiple hypothesis testing. In this case, the adjusted deviance p-value is given by

$$\text{p-value}_{adj, \mathcal{B}} = \max\left\{M \cdot P(\chi_m^2 > d_{(m)}), 1\right\} \quad (14)$$

Finally, the post-selection K-statistic specifies as

$$K_{(m)} = \max_{j=1, \dots, m} n \hat{\theta}_{(j)}^2,$$

where m is the value which maximises the BIC in (12), and let $k_{(m)}$ be the value of $K_{(m)}$ observed on the data. A post-selection adjustment for the respective p-value can be implemented as formalised in Theorem 1. The respective proof is given in the Appendix B.

Theorem 1. As $n \rightarrow \infty$, an upper bound for the limit of $P(K_{(m)} \geq k_{(m)} | H_0)$ is

$$\text{p-value}_{adj, \mathcal{K}} = 1 - P(\chi_1^2 \leq k_{(m)})^M. \quad (15)$$

A comparison in terms of power and type I error of tests based on (13), (14) and (15) is postponed to Section 4.3.

4 STATISTICAL DATA ANALYSIS OF RT Cru

Here we describe how smooth tests can be implemented to thoroughly study the X-ray spectra of RT Cru. As outlined in Section 1, our strategy is that of conducting a separate analysis on each of the 9 wavelength bands listed in Table 1.

Specifically, in Section 4.1, we first demonstrate how the shape of the background can be extracted on the basis of the information contained in the source-free, background-only dataset. Second, in Section 4.2.2, we apply the same method to the source spectrum. This step allows us to determine whether a significant difference can be established between the source spectrum and the background spectrum, without imposing any distributional assumption on potential signals. Third, if no difference can be detected, in Section 4.2.3 we complement our analysis by means of Likelihood Ratio Tests (LRTs)

to assess for the presence of the spectral lines listed in Table 1. For both smooth tests and the LRTs, adequate adjustments for multiple hypothesis testing are implemented in order to control for the probability of a false discovery across all the regions of the spectrum being tested. The statistical properties of the testing procedures considered are investigated in Section 4.3. Finally, since no spectral line is detected, we set upper limit on the counts necessary for a detection in each of the regions considered.

4.1 Data-driven Background Corrections

When assessing the validity of a postulated background model and implementing adequate data-driven corrections, it is necessary to ensure the size of the source-free sample considered is sufficiently large to reduce the uncertainty associated with the estimation of the background model. Therefore, here we proceed to combine the regions of interest W_r in Table 1 into five ‘‘calibration’’ intervals C_w , $w = 1, \dots, 5$, and defined as in Table 4.

The choice of considering larger regions ensures that, for each of the newly constructed calibration intervals C_3 - C_5 considered, the corresponding source-free sub-sample includes at least 20,000 events.

The background is assumed to be flat over the entire search area and thus we proceed by testing this assumption on each sub-region by means of the tools described in Section 3. The adjusted p-values to test the uniformity of the background, for each calibration region C_w , $w = 1, \dots, 5$ have been computed as in (13), (14) and (15). The results are summarised in Table 4.

In three out of the five calibration regions in Table 4, the data distribution is consistent with the uniform model (the adjusted p-values are all equal to one). Whereas on C_2 and C_4 , the flat background model is rejected. Therefore, we proceed to implement a data-driven correction for them as described in Section 3.2. The newly estimated background densities are

$$\begin{aligned} \hat{b}_{C_2}(x) &= 0.2424 - 0.0038x, & x \in [5.5, 10.2] \text{ \AA}, \\ \hat{b}_{C_4}(x) &= 1.3994 - 0.0250x, & x \in [14.6, 17.4] \text{ \AA}. \end{aligned} \quad (16)$$

Our ultimate goal is to detect signals over the regions of interest, W_r , defined as in Table 1, it is, therefore, necessary to convert the re-calibrated background densities obtained for C_2 and C_4 into corrections for the background distribution over W_r , $r = 1, \dots, 9$.

Specifically, let B_{W_r} be the true (unknown) background distribution on region W_r and let b_{W_r} be its density. We denote with \hat{b}_{W_r} our estimate of b_{W_r} . Since no deviation from uniformity was observed over C_1, C_3 and C_5 , no background update was performed on the regions W_1, W_3, W_6, W_7, W_8 and W_9 . Hence we set,

$$\hat{b}_{W_r}(x) = \frac{1}{u_r - l_r}, \text{ for } r = 1, 3, 6, 7, 8, 9,$$

with l_r and u_r be, respectively, the lower and upper bounds of the wavelength range of region W_r . Whereas, we exploit (16) to derive the newly calibrated background models for regions W_2, W_4 and W_5 . Since W_2 and C_2 coincide, we set $\hat{b}_{W_2}(x) = \hat{b}_{C_2}(x)$ and defined in (16). Whereas, the background models for regions W_4 and W_5 are

$$\begin{aligned} \hat{b}_{W_4}(x) &= 2.4749 - 0.0441x, & x \in [14.6, 15.15] \text{ \AA}, \\ \hat{b}_{W_5}(x) &= 1.1900 - 0.0212x, & x \in [16.2, 17.4] \text{ \AA}, \end{aligned} \quad (17)$$

and they have been derived as described in Appendix C.

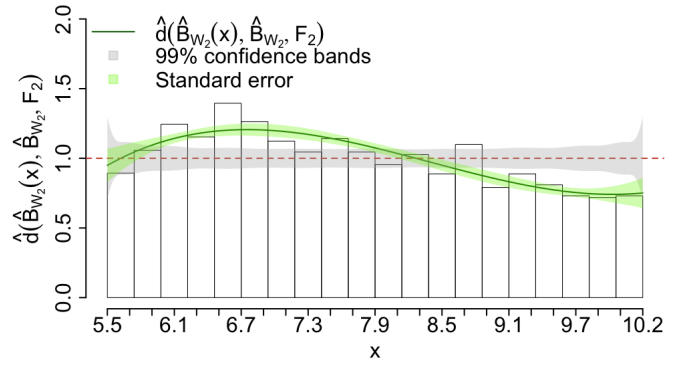


Figure 3. Comparison density plot and histogram of the transformed physics data, $u_i = \hat{B}_{W_2}(x_i)$, $i = 1, \dots, 3311$, for region W_2 . The hypothesised model is the corrected background density $\hat{b}_{W_2}(x)$ in (17). The estimated comparison density in (19) is displayed using a green solid line. The green bands are the estimated standard errors of $d(\hat{B}_{W_2}(x); \hat{B}_{W_2}, F_2)$ obtained by simulating samples from the estimator in (19). The red dashed line corresponds to the null hypothesis that $d(\hat{B}_{W_2}(x); \hat{B}_{W_2}, F_2) = 1$, i.e., the data distribution on W_2 is not significantly different from the estimated background model $\hat{b}_{W_2} = \hat{b}_{C_2}$ in (16). The grey bands correspond to the 99% confidence bands under the null. The plot suggests that there exists a significant departure of the true data distribution from $B_{W_2}(x)$, within the range of $x \in [6.1, 7.9] \text{ \AA}$.

4.2 Signal Detection via Smooth Tests and LRTs

4.2.1 Testing multiple regions and adequate corrections

Let F_r be the true distribution from which the observations in the source sample were generated over region W_r , $r = 1, \dots, 9$, and denote with f_r its density. We assume that, if no signal is present, the true density f_r is well approximated by our background estimate \hat{b}_{W_r} obtained as in Section 4.1. Hence, in Section 4.2.2, we employ smooth tests to assess if significant deviations from \hat{b}_{W_r} occur on any of the nine regions considered. For regions where no significant departure from the background model is detected, we will proceed with a thorough search for spectral lines via LRTs, as described in Section 4.2.3.

Notice that, in both our smooth tests and LRTs analyses, multiple tests are conducted simultaneously over different regions. It is therefore necessary to correct the resulting p-values for multiple hypotheses testing in order to ensure that the probability of a false discovery across the entire spectrum is no larger than the predetermined α . Hereinafter, we will refer to the latter as the *global significance level*.

Under the hypothesis of independence of the tests being conducted, α relates to the *local significance level*, α_r , of incorrectly rejecting the background-only hypothesis on region W_r in that

$$\alpha = 1 - \prod_{r=1}^R (1 - \alpha_r).$$

The reader is directed to Algeri et al. (2016) for a self-contained review on the problem of multiple hypothesis testing in searches for new physics also referred to in physics literature as *look-elsewhere effect*.

In our setup, since the regions in which our spectrum is divided are non-overlapping, we can assume independence among the tests performed separately on each of them. Hence, we can adequately adjust the corresponding p-values by relying on Sidak’s correction (e.g., Kuehl 2000, Sec 3.4). Specifically, letting p_r be the (smooth

Combined regions (C_w)	Wavelength range in Å	m	Bonferroni (Sidak)	K (Sidak)	Naive (Sidak)	N_w
C_1	1.65-2.05	0	1.0000 (1.0000)	1.0000 (1.0000)	1.0000 (1.0000)	6879
C_2	5.5-10.2	1	3.7687e-10 (1.8843e-09)	3.7687e-10 (1.8843e-09)	3.6797e-06 (1.8398e-05)	75699
C_3	11.5-13.0	0	1.0000 (1.0000)	1.0000 (1.0000)	1.0000 (1.0000)	22809
C_4	14.6-17.4	1	0.0004 (0.0020)	0.0004 (0.0020)	0.0796 (0.3396)	41186
C_5	18.5-23.0	0	1.0000 (1.0000)	1.0000 (1.0000)	1.0000 (1.0000)	63372

Table 4. Summary of our background correction results for each calibration region. The first two columns are the combined calibration regions and corresponding combined wavelength ranges. The third column reports the number, m , of coefficients selected out of $M = 10$, for each of the combined regions considered. The p-values adjusted for post-selection using the Bonferroni, K, and naive corrections and corrected for multiple hypothesis testing via Sidak (see 18) are given in the fourth, fifth, and sixth columns, respectively. The size of the source-free sample N_w for each of the combined regions $w = 1, \dots, 5$ are given in the last column.

Regions of interest (W_r)	m	Bonferroni (Sidak)	K (Sidak)	Naive (Sidak)
W_1	3	0.0001 (0.0011)	0.0071 (0.0397)	0.0045 (0.0621)
W_2	3	1.0816e-18 (1.0817e-17)	2.7907e-15 (2.9976e-14)	3.3306e-15 (2.4980e-14)
W_3	0	1.0000 (1.0000)	1.0000 (1.0000)	1.0000 (1.0000)
W_4	0	1.0000 (1.0000)	1.0000 (1.0000)	1.0000 (1.0000)
W_5	0	1.0000 (1.0000)	1.0000 (1.0000)	1.0000 (1.0000)
W_6	0	1.0000 (1.0000)	1.0000 (1.0000)	1.0000 (1.0000)
W_7	0	1.0000 (1.0000)	1.0000 (1.0000)	1.0000 (1.0000)
W_8	0	1.0000 (1.0000)	1.0000 (1.0000)	1.0000 (1.0000)
W_9	0	1.0000 (1.0000)	1.0000 (1.0000)	1.0000 (1.0000)

Table 5. Summary of our signal detection results for each region of interest using smooth tests. The second column shows the number, m , of coefficients selected out of $M = 10$, for each of the nine regions considered. The p-values adjusted for post-selection using the Bonferroni, K, and naive corrections and corrected for multiple hypothesis testing via Sidak (see 18) are given in the third, fourth and fifth columns, respectively.

Regions of interest (W_r)	Local p-values	Sidak's correction
W_3	0.4810	0.9899
W_4	0.1143	0.5724
W_5	0.3247	0.9359
W_6	0.0385	0.2402
W_7	0.2612	0.8799
W_8	0.5000	0.9922
W_9	0.5000	0.9922

Table 6. Local P-values and adequate multiple hypothesis testing adjustments when testing for spectral lines via LRTs.

test or LRT) p-value obtained for region r , the corresponding Sidak's correction is

$$p_r^{\text{Sidak}} = 1 - (1 - p_r)^R \quad (18)$$

with R being the total number of regions being tested. Notice that the same corrections have also been implemented in Table 4 when assessing the validity of flat backgrounds on the source-free sample.

4.2.2 Signal detection via smooth tests

Similarly to Section 4.1, we rely on the deviance and the K-statistics (suitably adjusted for post-selection, as described in Section 3.3) to perform our tests.

The discovery results on each of the regions of interest are summarised in Table 5. The second column of the Table 5 corresponds to truncation point, m , selected via the *BIC* criteria in (12), when considering a maximum of $M = 10$ coefficients. The Sidak adjusted p-values calculated as in (18) with $R = 9$ are reported in parenthesis. Recall that our estimator and test statistics are constructed by sorting the estimated coefficients $\hat{\theta}_{(j)}$ in (4). Hence, choosing m to

be the point of truncation implies that inference and estimation are performed considering only the m largest estimated coefficients.

For regions W_1 and W_2 , the Bonferroni and K adjusted p-values are smaller than the global significance level $\alpha = 0.05$ even after implementing Sidak's correction. Whereas, the p-values adjusted for post-selection by means of the naive method, only detect significant deviations over region W_2 . As discussed in detail in Section 4.3, this result is not surprising since the naive approach is the most conservative among the three methods considered. The adjusted p-values for the remaining regions are all equal to one. This implies that our smooth tests analysis allows us to claim that deviations from the background occur only on regions W_1 and W_2 .

The results obtained on the region W_1 are consistent with those of Luna & Sokolowski (2007). These are known features, arising in inner accretion disk perhaps, and their detection here is a confirmation that the method is working.

To gain a better understanding of the nature of the deviation from the background model detected on region W_2 , we rely on the so-called *Comparison Density plot* or *CD-plot* (e.g., Algeri & Zhang 2021) shown in Figure 3. The CD-plot allows us to visualise where the data distribution deviates significantly from the hypothesised distribution (in our case, the re-calibrated background density). It displays the estimated comparison density (dark green solid line) and which, for region W_2 specifies as

$$\hat{d}(u; \hat{B}_{W_2}, F_2) = 0.9500 + 2.1577u - 5.2749u^2 + 2.9179u^3 \quad (19)$$

where $u = \hat{B}_{W_2}(x)$. Whereas, the green bands are the standard errors of $\hat{d}(\hat{B}_{W_2}(x); \hat{B}_{W_2}, F_2)$ obtained by simulating from the estimator in (19) as described in Algeri & Zhang (2021). The grey bands correspond to the 99% confidence bands under the null hypothesis of background only. If the estimated comparison density is within the confidence bands, over the entire range considered, we conclude that there is no significant departure from the background model.

Conversely, we expect significant deviations to occur in regions where the estimate lies outside the confidence bands. It is worth emphasising that the CD-plot provides us a representation of the data in the quantile domain; that is, it displays the transformed data $u_i = \widehat{B}_{W_2}(x_i)$, $i = 1, \dots, 3311$, and their estimated density. Such representation ensures that the most substantial departures of the data distribution from the expected model are magnified and those due to random fluctuations are smoothed out. More details on the construction and discussion of the CD-plot can be found in [Algeri & Zhang \(2021, Algorithm 1\)](#) and [Algeri \(2020, Section V A\)](#).

For the specific case of Region W_2 , the CD-plot in [Figure 3](#) suggests that significant departures from \widehat{b}_{W_2} occur within the range of $x \in [6.1, 7.9] \text{ \AA}$. This detection, however, cannot be attributed to any known spectral features, and it corresponds to the signature of the Chandra optics Iridium absorption edge and is detectable because we are not assuming a particular spectral model here. It is worth pointing out that the departure below one at $x \gtrsim 9.1 \text{ \AA}$ is due to the fact that, since the $\widehat{d}(\widehat{B}_{W_2}(x); \widehat{B}_{W_2}, F_2)$ is the estimate of a density function, its integral is ≈ 1 (adequate corrections to ensure that the integral of the resulting estimate is exactly 1 can be implemented as described, for instance, in [Algeri & Zhang \(2021\)](#)). It follows that any peak or departure above 1 is compensated by a departure below one over the remaining portion of the search region (in our case, for $x \gtrsim 9.1 \text{ \AA}$).

4.2.3 Signal detection via LRTs

To further investigate the possibility of undetected spectral lines in regions W_3 - W_9 we proceed by implementing an inferential analysis based on LRTs.

As noted in the introduction, the main advantage of smooth tests is that they allow us to detect deviations from the background occurring at the m “most significant” directions identified by the BIC criterion in (12). Therefore, they are completely model-independent, that is, they do not require us to specify the position of the spectral lines or a model for their shape. Nonetheless, when such information is available, one can assess if deviations from the background occur in the direction of the specified signal model by means of the LRT, which is known to be the most powerful test when a model for the signal is provided.

We begin by assuming that, if a spectral line is present on region W_r , its density is¹

$$s_r(x, \tilde{\mu}_r) = k(\tilde{\mu}_r) \left\{ 1 + \left[\frac{(x - \tilde{\mu}_r)}{0.05} \right]^2 \right\}^{-2.5} \quad (20)$$

with

$$\tilde{\mu}_r \sim N(\mu_r, 0.005^2)$$

where $\tilde{\mu}_r$, $r = 3, \dots, 9$, is the expected signal location (see column 4 of [Table 1](#)) and $k(\tilde{\mu}_r)$ is the normalising terms depends on the random variable $\tilde{\mu}_r$.

We can then specify a suitable model for regions W_3 - W_9 as

$$q_r(x, \eta_r, \tilde{\mu}_r) = (1 - \eta_r) \widehat{b}_{W_r}(x) + \eta_r s_r(x, \tilde{\mu}_r) \quad (21)$$

¹ This is the so-called line response function (LRF) that describes the response of a grating to an infinitesimally narrow line. It is empirically modeled as a modified Lorentzian, also called a Beta-profile; see Equation 9.1 of the *Chandra Observatory Proposers' Guide*, https://cxc.harvard.edu/proposer/POG/html/chap9.html#tth_sEc9.3.3

where \widehat{b}_{W_r} is the background model adequately corrected, as needed, following the method described in [Section 4.2](#), whereas η_r is the relative intensity of the expected signal. To test if a spectral line with density s_r is present on region W_r we test the hypotheses

$$H_0 : \eta_r = 0 \quad \text{versus} \quad H_1 : \eta_r \in (0, 1], \quad r = 3, \dots, 9 \quad (22)$$

by means of the test statistic

$$\lambda_r = -2 \sum_{i=1}^n \left\{ \log \widehat{b}_{W_r}(x_i) - \max_{\eta_r \in (0, 1]} \log q_r(x_i, \eta_r, \tilde{\mu}_r) \right\}. \quad (23)$$

Notice that the parameterisation in (21) implicitly assumes that, under the alternative hypothesis, the true density, f_r , is equal to q_r . Therefore, tests based on such model are unable to capture any deviation from $\widehat{b}_{W_r}(x)$ other than the one in the direction of $s_r(x, \tilde{\mu}_r)$ (hence the analysis in [Section 4.2.2](#)).

Under suitable regularity conditions (e.g., [Algeri et al. 2020](#)), the null distribution of λ_r in (23) can be approximated by a χ^2 ([Wilks 1938](#)). However, since η_r in (21) lies on the boundary of its parameter space, under H_0 , the χ^2 approximation is no longer valid. Nonetheless, in this setting, the null asymptotic distribution of the LRT is known to be a zero 50% of the times and it is χ_1^2 the remaining 50% ([Chernoff 1954](#)). Therefore, it is sufficient to divide by a factor of two the “usual” p-value obtained using the χ_1^2 approximation.

The results of the LRT for each of the seven regions considered are summarised in [Table 6](#). In the second column, we report the local p-values, that is, the p-values obtained without adjusting for multiple hypothesis testing whereas the global p-values adjusted by means of Sidak’s correction in (18) with $R = 7$ are reported in the third column. All the regions apart from W_6 have local p-values larger than 0.05. For region W_6 , the local p-value 0.0385. However, once adequately adjusted via Sidak’s correction, the p-value for W_6 is no longer significant. This result emphasises the importance of implementing adequate corrections when conducting multiple test simultaneously to avoid false discoveries claims.

4.3 Statistical Properties and Construction of Upper Limits

In order to confirm the validity of the analyses performed in [Sections 4.2.2-4.2.3](#), it is important to investigate the statistical properties (power and probability of type I error) for each of the inferential procedure considered. We will then exploit the power curves obtained to construct suitable upper limits as prescribed in [Kashyap et al. \(2010\)](#).

We investigate the power of the proposed statistical tests by simulating Monte Carlo samples from q_r in (21) for different intensity levels η_r . The size of each simulated dataset is the same as that of the original sample observed on the seven regions considered (i.e., n_r with $r = 3, \dots, 9$ in [Table 1](#)). Using the simulated data, we implement the methods described in [Section 3](#) as well as the LRT procedure discussed in [Section 4.2.3](#). When the true value of η_r is non-zero, the null hypothesis in (22) is correctly rejected if the p-value is smaller than the pre-specified significance level. We repeat this process 5000 times, and at each replicate, we record the number of rejections of the null. The proportion of rejections corresponds to the simulated power for the (non-zero) values of η_r fixed when conducting the simulation. We repeat the simulation for different values of η_r in order to generate a series of power curves, one for each region considered. The latter is displayed in [Figure 4](#). The same analysis is also repeated by adjusting the respective p-values for multiple hypothesis testing via Sidak’s correction in (18) at each replicated of the sim-

ulation. As expected, adjusting for multiple hypothesis testing leads to a reduction of the power. Not surprisingly, the power of the LRT is higher than any other procedure considered. That is because, smooth tests do not require the specification of the signal model and simply assess for the presence of deviations from the background.

The probabilities of type I error for each of the procedures considered (obtained by setting $\eta_r = 0$) are reported in Tables D1-D2. The simulated type I error using Bonferroni adjustment for the deviance statistic often exceeds the significance level of 0.05 in the context of local analysis. It also exceeds the significance level $\alpha_r = 0.0073$ in the global analysis; that is when setting the probability of false discovery across all the seven regions to be $\alpha = 0.05$. Conversely, the K-statistic and the naive post-selection adjustment for the deviance perform well in controlling the specified significance level even though the naive adjustment appears to be excessively conservative (the respective probability of type I error is always zero in the global analysis). This is reflected also in the power curves reported in Figure 4. The naive approach is the most conservative among the three, whereas Bonferroni exhibits the highest power.

Finally, upper limits are constructed by inverting the power curves of the LRT at 50% and 90% and multiplying the resulting η_r value for the sample size, n_r (see Table 1) of the discovery region W_r , for $r = 3, \dots, 9$. The results are summarised in Table 7. We can interpret the Sidak adjusted upper limits as the number of samples from the expected signal needed to achieve the specified power when testing simultaneously regions W_3 - W_9 . For example, for region W_3 , our 50% upper limit computed using the LRT after Sidak correction is 40 (39.42). This tells us that if a spectral line at position 12.131 Å was present, we would need 40 events in this location (out of the 730 observed in the entire W_3 region) to be able to detect such spectral line with power 50%, while simultaneously looking for spectral lines in the regions W_4, \dots, W_9 . Whereas, if we were interested in designing a future observation targeting solely region W_3 , our 50% upper limit computed using the (local) LRT is 30 (29.93). This tells us that if a spectral line at position 12.131 Å was present, we would need 30 events at such location to detect it with power 50%, and assuming that no other test on other regions is conducted at the same time. Similar interpretations can be given to the 90% upper limits and for other regions.

For the sake of comparison, the upper limits obtained by means of smooth tests are reported in Tables D3-D4. Not surprisingly, since smooth tests do not rely on the specification of a model for the signal, they are more conservative than the LRT. For example, for region W_3 , the 50% upper limits computed using the Bonferroni, K-statistic and the naive methods, and adjusted via Sidak for multiple hypothesis testing lead to 53, 64, and 68 events, respectively.

5 DISCUSSION

5.1 Advantages and Limitations

We have developed a novel method to detect weak signals distinct from a smooth background in high-resolution photon counting spectra. This approach anticipates difficulties likely to be encountered in the coming era of calorimeter spectra. The method is implemented to work with unbinned photon lists that allows the full available spectral resolution to be used, though a modification to use binned spectra is viable from an algorithmic perspective and it is the subject of future work.

The statistical methodology presented here is particularly advantageous at high resolution because a precise specification of the

source model spectrum is often not possible as the information available in the data usually exceeds that in the models proposed. Here we show that one can indeed exploit this phenomenon by **modeling** and estimating the “gap” between the (potentially **misspecified**) model available and the true spectrum using smooth functions like shifted Legendre polynomials. On this note, it is worth emphasizing that, as proven in Algeri (2020), the closer the postulated model is to the truth, the more accurate (less biased) is the estimate of the latter. It follows that, in principle, one could avoid specifying a model for the spectrum and estimate it by means of smooth functions. Nonetheless, if a model is available (even if misspecified), it should be used in order to reduce the gap between the proposed model and the truth.

The implementation currently ignores spectral calibration products like the effective area and the redistribution matrices, and therefore cannot be applied to CCD resolution spectra. Furthermore, the method relies on a comparison between the smooth model description of the source-free background and the source+background datasets, so it cannot be applied to cases where the background is contaminated by the source or where the background is not smoothly varying.

5.2 Inferences based on RT Cru analysis

5.2.1 Domain of applicability

We first note that our method easily detects the presence of significant source emission in passband W_1 . This is not surprising, as these lines have been identified and analyzed by several studies (e.g., Luna & Sokoloski (2007) resolved it clearly in HETGS+ACIS-S spectra; and Danehkar et al. (2021) successfully modeled the triplet in the same dataset that we use). The chance that a random fluctuation can produce a detectable departure from the background is assessed as $p \lesssim 10^{-2}$ after accounting for multiple hypothesis tests (see Table 5). This serves as a validation of the method, in that a line complex known to exist is correctly found.

An important characteristic of our method is that it is not limited to narrow lines. If the source spectrum has a different shape compared to the background spectrum, we expect that to be detected, i.e., the method allows for a differentiation between the continuum and the background. This was achieved serendipitously in passband W_2 , where the existence of a feature is flagged with high significance ($p \ll 10^{-10}$; see Table 5). The detected feature (see Figure 2) is a characteristic of the response of the *Chandra* mirror coating, exhibiting an edge due to the absorption of incident photons by Iridium. Such features are usually not visible in residuals in standard spectral analyses because the modeling directly incorporates the sensitivity of the telescope system and suitably weights the incident photon spectrum. Because our method does not include such calibration products, it can be used to locate and study such features, incorporating known calibration (as is done for line emission in Equations 20, 21), thus potentially providing independent measures of uncertainty on the calibration.

5.2.2 Thermal line emission

We have explored the possibility of detecting emission from some prominent soft X-ray emission lines (Table 1; see also Section 2.1) and find that in no case are any of the lines we searched for detectable. Here we compare the model predicted counts obtained using the spectral model of Danehkar et al. (2021) with a nominal estimate of background corrected counts estimate obtained via a Bayesian estimate (as in Freeman et al. 2002), with the 50% upper

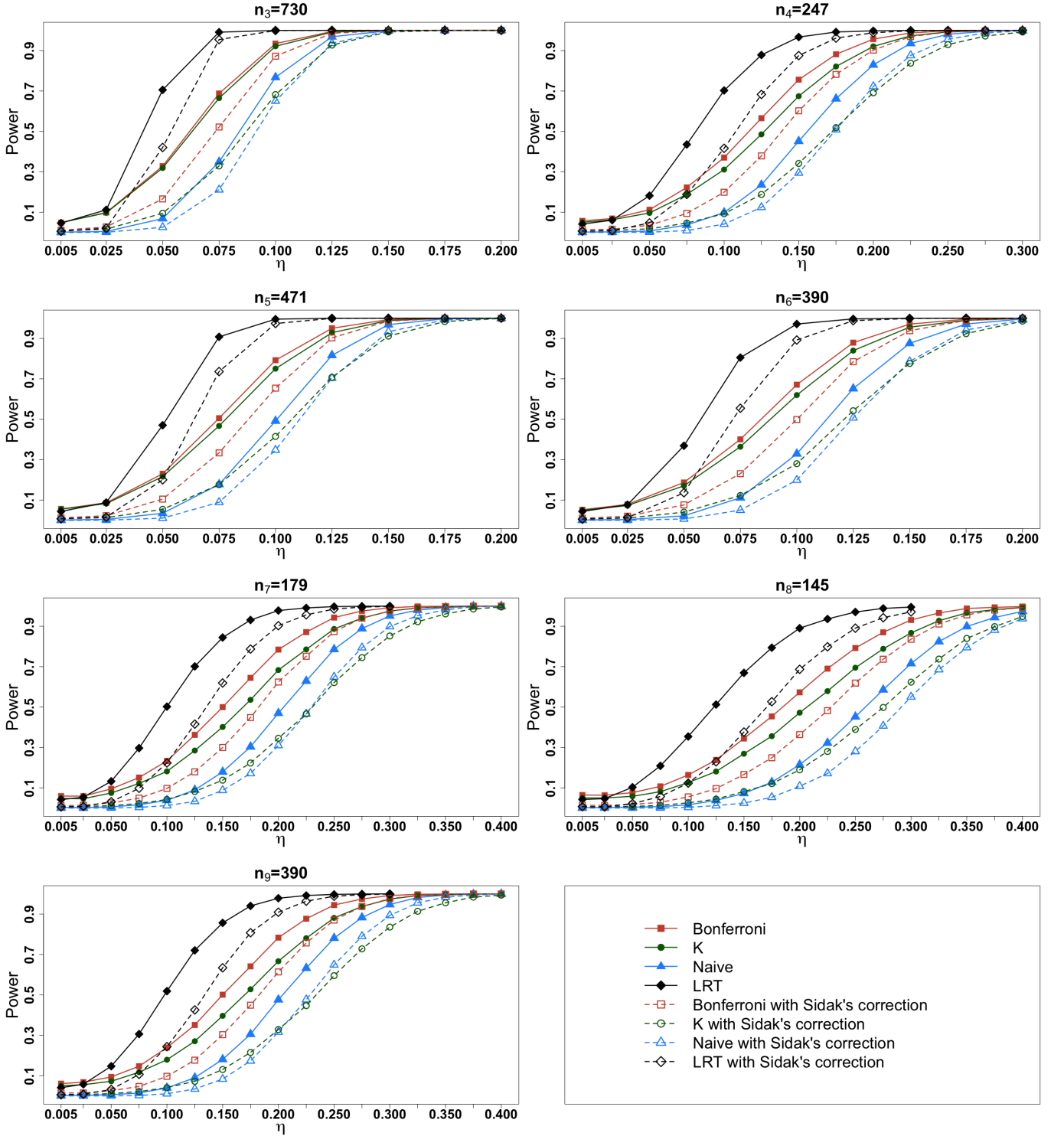


Figure 4. Simulated power curves for regions W_3 – W_9 . Red-square and blue-triangle lines correspond to the power curves for the deviance adjusted for post-selection via Bonferroni and the naive approach, respectively. The green-circle lines are the power curves for the K-statistic suitably adjusted for post-selection. The black-diamond lines are the power curves for the LRT. The solid lines correspond to the local power curves, with $\alpha_r = 0.05$, for each $r = 3, \dots, 9$. The dashed lines are the power curves adjusted for multiple testings using Sidak's correction to ensure a global significance of $\alpha = 0.05$ (local significance $\alpha_r = 0.0073$, for each $r = 3, \dots, 9$).

Regions (W_r)	50% upper limits via LRT		90% upper limits via LRT	
	Local	Sidak adjusted	Local	Sidak adjusted
W_3	29.93	39.42	48.91	53.29
W_4	20.00	26.43	32.36	39.52
W_5	24.02	30.14	35.32	43.80
W_6	22.62	28.08	34.71	39.39
W_7	17.90	24.17	29.71	35.98
W_8	17.84	24.80	30.30	36.25
W_9	37.83	21.87	63.57	76.83

Table 7. 50% and 90% upper limits on different regions using the LRT, with and without Sidak’s correction. The 50% upper limits are calculated by the proportion of the expected lines η to achieve the power 0.5 (solid line in Figure 4) times the sample sizes n_r . Similarly, the 90% upper limits are calculated by the proportion of the expected lines η to achieve the power 0.9 times the sample sizes n_r .

	Shifted lines [\AA]	Local p-values	Sidak’s correction	LRT 50% Upper limits	LRT 90% Upper limits	Sidak’s LRT 50% Upper limits	Sidak’s LRT 90% Upper limits
W_4	14.908	0.5000	0.9921	20.00	32.60	26.92	39.77
W_5	16.930	0.0017	0.0118	24.54	34.85	30.14	43.80

Table 8. Local p -values for the LRT and adequate multiple hypothesis testing adjustments when investigating the presence of the 16.93 \AA emission line in W_5 .

limits obtained using smooth tests and post-selection adjustments (Section 4; Table 7):

W_3 : This passband is centered on the Ne X resonance line at 12.14 \AA . The model predicts ≈ 16 counts in this region, and a measurement of the counts over the width of the LRF yields an estimate of ≈ 20 counts, with a 68% uncertainty interval of $\approx \pm 10$. This would normally be considered a good match between model and data, but the upper limit at this location is ~ 30 counts, increasing to ~ 40 counts when corrections due to multiple hypotheses testing are included, and we conclude that the line is not detectable. This assessment is supported by a visual inspection of the observed counts spectrum, where an enhancement in counts at the location of the line is not apparent.

W_4 and W_5 : The dominant features in these bands are expected to be from the Fe XVII lines at 15.014 \AA , 17.051 \AA and 17.096 \AA . Note that these lines have peak emissivity at ≈ 5 MK, whereas the best-fit spectral model suggests a plasma temperature of ≈ 14 MK. The emissivities at such high temperatures are reduced by a factor of 30, but they remain the strongest lines from a thermal spectrum and have approximately similar intensities. The predicted counts from the best-fit model is ≈ 10 counts in each, and the measured values are ≈ 20 and ≈ 6 counts in W_4 and W_5 respectively. These estimates are prima facie inconsistent with theoretical expectations, though the posterior distributions of the intensities do overlap. The local upper limits are 20 and 24 counts, increasing to 26 and 30 counts at the 50% level (see Table 7) after accounting for multiple hypotheses, for W_4 and W_5 respectively. This suggests that the 15 \AA line is a borderline detectable feature, but the 17 \AA lines are not detected. However, notice that in the counts spectrum in Figure 2, there is a relatively strong feature at ≈ 16.93 \AA , about 2100 km s^{-1} blueward of 17.051 \AA (marked with a brown cross-hatch). We find that the feature is detected with a significance of $p \lesssim 0.002$ locally and at $p \lesssim 0.012$ after multiple hypothesis correction (see Table 8), with a 50% upper limit < 25 counts. The estimated signal strength for this feature is $16.9 \text{ }_{8.5}^{26.9}$ counts (the bounds represent 68% HPD uncertainty interval as in Table 2), consistent with the putative upper limit. Inner accretion disk velocities of $\sim 10^3$ km s^{-1} are plausible for symbiotic variables (see, e.g., Reimers & Cassatella 1985), though the required shift here is twice as much. A hot spot that can achieve such a large blue shift would be located at a height of $\approx 0.06 R_\odot$ above a 1.4 M_\odot white dwarf, which is not infeasible. But

if this were a blue-shifted Fe XVII $\lambda 17.051$ line, we should expect its 15 \AA counterpart to also be similarly blue shifted. The location of this putative blue-shifted 15 \AA line is also marked with a brown cross-hatch in the W_4 panel in Figure 2. We find no detectable feature at this location, with a multiple-hypothesis corrected 50% upper limit at < 27 counts (Table 8; the estimated counts are $0 \text{ }_{>0}^{8.2}$). We thus conclude that the feature at 16.93 \AA is *not* a blue-shifted thermal line. We discuss its possible origin further in Section 5.2.3 below.

W_6 : The strongest feature in this passband is the O VIII resonance line at 18.96 \AA . As can be seen in Figure 2, there is an apparent enhancement at where the line is expected to be, though the predicted model counts are more than $2\times$ smaller compared to the estimated counts, and indeed the predicted counts value falls outside the 68% uncertainty bounds (Table 2). Interestingly, the local upper limit shows that the deviation is significant with $p < 0.05$, but when corrections due to multiple hypothesis tests are included, there is no significant evidence for a detection. The 50% upper limit is < 28 , and we conclude that the data are not of suitable quality to constrain the Oxygen emission.

W_7 - W_9 : These three bands include the He-like density sensitive triplet of O VII at 21.6, 21.8, and 22.1 \AA . We find no evidence for a detection of any of the lines, with the corrected $p \approx 1$ in all three cases, and with 50% upper limits in the 21 – 24 counts range. However, this case provides a cautionary illustration of the pitfalls of ignoring detectability. The nominal estimates of the counts in each of the lines shows that the intercombination line at 21.8 \AA has a brightness of ≈ 10 counts, higher than both the resonance and forbidden line brightnesses. Without the upper limits analysis demonstrating that none of the lines are detectable, it is easy to over-interpret the high brightness estimate of the intercombination line as indicative of a very high density ($\gg 10^{13} \text{ cm}^{-3}$; see, e.g., Smith et al. 2001) in the emitting plasma. While the presence of such high densities cannot be formally excluded, the current dataset is of insufficient quality to place a definitive constraint. Observations with new observatories like XRISM, Athena, or LEM are necessary to resolve this question.

5.2.3 The Origin of the 16.93 \AA Feature

The hard emission in the 6-7 keV range likely originates close to the accretor. The 6.4 keV Fe K α line could originate from a region of the boundary layer of the accretion disk or in a bright

spot on the disk; The 6.7 keV and the 7 keV, can be attributed to He-like and H-like iron emission lines, and could be produced via photoionization and collisional ionization/excitation mechanisms in the hot plasma, either in the vicinity of the WD or the inner-jet region, or both (see, e.g., Kennea et al. 2009, Karovska et al. 2010, Eze 2014). We speculate that the same photoionization or reflection spectrum photon reprocessing could be the source of the line feature detected at 16.93 Å. Several plausible candidate ionic species ranging from Fe XIII to Fe XIX exist in the XSTAR (Kallman 1999) line list within $\approx 500 \text{ km s}^{-1}$ of the detected line. The reflection spectrum model `xillver` (García et al. 2013) shows the existence of emission localized at 16.93 Å for flat incident spectra ($\Gamma \approx 1-1.2$), moderate Fe abundances ($A_{\text{Fe}} \approx 0.5-1$), ionization ($\log \xi \approx 2-3$). Intriguingly, a feature at the same location was found by Hemphill et al. (2021) in the *Chandra* LETG spectrum of the ultracompact X-ray binary 4U 1626–67; they are also unable to identify the line, and suggest a photoionized emission as the origin. Unlike the double-peaked emission that Hemphill et al. find that is reminiscent of an accretion-disk origin, the profile of the line in RT Cru is sharply single-peaked, suggesting an origin in a hot spot or an inner jet. A detailed study of the origin of this line, and a search for other such lines is beyond the scope of both this article and the *Chandra* dataset; we expect that observations obtained with calorimeter resolutions will confirm the presence of such lines and lead to a better understanding of the emission from RT Cru and other symbiotics.

6 SUMMARY

We present a method designed to correctly analyze high-resolution spectra affected by high background. The method is currently implemented for photon lists, but extensions to binned spectra such as those obtained by XMM/RGS are possible in principle and are the subject of future work. We first characterize the background and determine whether the background-contaminated source spectrum differs significantly in its shape over any passband. This allows us to detect both line emission as well as continuum variations. We properly correct for multiple hypothesis tests, and where a spectral line is not detected, we place upper limits on the source intensity. From a statistical perspective, in addition to the novel analytical framework presented here, we introduce a new test statistic to perform smooth tests and adequate post-selection inferential adjustments. The latter are obtained by simply inverting the power function of our post-selection adjusted smooth tests and obtained via Monte Carlo simulations.

We apply this method to the *Chandra* LETGS+HRC-S spectrum of the symbiotic star RT Cru. Because of the high background, traditional techniques designed to detect and identify lines and compute fluxes are unfeasible for these data. Consequently, a global fit was carried out by Danehkar et al. (2021) using a power-law and a thermal component, supplemented by Gaussian lines to model the Fe K α region. We first validate our method by confirming the detection of the Fe-line triplet in the 6–7 keV region, and further demonstrate the ability of the method to find variations in the continuum spectrum by detecting the Iridium M edge present due to the mirror coating in all *Chandra* observations.

Since the clear detection of low energy spectral lines would be an important diagnostic for the emission mechanisms that operate in symbiotic systems, we have employed smooth models and smooth tests to correct, when needed, the uncertain background model and to determine whether source spectra show distinct differences in shape compared to the background in several wavelength bands

where spectral lines are expected to be present. None of the expected thermal lines are detected, and the upper limits are all larger than the predicted model counts. With the analysis of the O VII He-like triplet, we illustrate how checking for detectability allows us to avoid mistakenly claiming that the emitting plasma is at high density. We thus conclude that the fitted model considered by Danehkar et al. (2021) is adequate in its overall characteristics to explain the emission from RT Cru.

We serendipitously and unambiguously detect emission in a line-like feature located at 16.93 Å, and conclude that it cannot be attributed to thermal plasma emission. We speculate that it is derived from a hitherto unmodeled photoionization of reflection spectrum component. Future observations with missions like XRISM (Ishisaki et al. 2022), Athena (Barret et al. 2022), etc., using calorimeter-level spectral resolutions and high effective areas are necessary to detect and model such processes.

ACKNOWLEDGEMENTS

Sara Algeri and Xiangyu Zhang are grateful for the financial support provided by the Office of the Vice President for Research at the University of Minnesota. Vinay Kashyap was supported by the NASA Contract NAS8-03060 to the *Chandra* X-ray Center. Margarita Karovska and Vinay Kashyap acknowledge support for this work provided via the *Chandra* grant GO5-16023X.

DATA AND CODE AVAILABILITY

The data and codes used for the analyses in Section 4 are available at the github site at <http://github.com/xiangyu2022/Symbiotic-Star-RT-Cru-Analysis>.

REFERENCES

- Algeri S., 2020, *Phys. Rev. D*, 101, 015003
 Algeri S., 2021, *Electronic Journal of Statistics*, pp 5570–5597
 Algeri S., Zhang X., 2021, *Journal of Computational and Graphical Statistics*, pp 1–12
 Algeri S., van Dyk D. A., Conrad J., Anderson B., 2016, *Journal of Instrumentation*, 11, P12010
 Algeri S., Aalbers J., Morå K. D., Conrad J., 2020, *Nature Reviews Physics*, 2, 245
 Barret D., et al., 2022, arXiv e-prints, p. arXiv:2208.14562
 Berk R., Brown L., Buja A., Zhang K., Zhao L., 2013, *The Annals of Statistics*, 41
 Bird A. J., et al., 2007, *ApJS*, 170, 175
 Chernoff H., 1954, *The Annals of Mathematical Statistics*, 25, 573
 Cieslinski D., Elizalde F., Steiner J. E., 1994, *A&AS*, 106, 243
 Cox D., 1975, *Biometrika*, 62, 441–444
 Danehkar A., Karovska M., Drake J. J., Kashyap V. L., 2021, *MNRAS*, 500, 4801
 Ducci L., Doroshenko V., Suleimanov V., Nikořajuk M., Santangelo A., Ferrigno C., 2016, *A&A*, 592, A58
 Eze R. N. C., 2014, *MNRAS*, 437, 857
 Fabbiano G., Elvis M., Paggi A., Karovska M., Maksym W. P., Raymond J., Risaliti G., Wang J., 2017, *ApJ*, 842, L4
 Fabbiano G., et al., 2019, *ApJ*, 870, 69
 Fabbiano G., Paggi A., Karovska M., Elvis M., Nardini E., Wang J., 2020, *ApJ*, 902, 49
 Freeman P. E., Kashyap V., Rosner R., Lamb D. Q., 2002, *ApJS*, 138, 185
 García J., Dauser T., Reynolds C. S., Kallman T. R., McClintock J. E., Wilms J., Eikmann W., 2013, *ApJ*, 768, 146

- Hemphill P. B., Schulz N. S., Marshall H. L., Chakrabarty D., 2021, *ApJ*, **920**, 142
- Ishisaki Y., et al., 2022, in den Herder J.-W. A., Nikzad S., Nakazawa K., eds, Society of Photo-Optical Instrumentation Engineers (SPIE) Conference Series Vol. 12181, Society of Photo-Optical Instrumentation Engineers (SPIE) Conference Series. p. 121811S, doi:10.1117/12.2630654
- Kallenberg W. C. M., Ledwina T., 1997, Journal of the American Statistical Association, 92, 1094
- Kallman T., 1999, XSTAR: A program for calculating conditions and spectra of photoionized gases, Astrophysics Source Code Library, record ascl:9910.008 (ascl:9910.008)
- Karovska M., Gaetz T. J., Carilli C. L., Hack W., Raymond J. C., Lee N. P., 2010, *ApJ*, **710**, L132
- Kashyap V. L., van Dyk D. A., Connors A., Freeman P. E., Siemiginowska A., Xu J., Zezas A., 2010, *ApJ*, **719**, 900
- Kennea J. A., Mukai K., Sokoloski J. L., Luna G. J. M., Tueller J., Markwardt C. B., Burrows D. N., 2009, *ApJ*, **701**, 1992
- Kolmogorov A., 1933, Giornale dell' Instituto Italiano degli Attuari, 4, 83
- Kraft R., et al., 2022, arXiv e-prints, p. arXiv:2211.09827
- Kuehl R. O., 2000, Designs of experiments: statistical principles of research design and analysis. Duxbury press
- Ledwina T., 1994, Journal of the American Statistical Association, 89, 1000
- Lopes de Oliveira R., Mukai K., 2019, *ApJ*, **880**, 128
- Luna G. J. M., Sokoloski J. L., 2007, *ApJ*, **671**, 741
- Luna G. J. M., et al., 2018, *A&A*, **616**, A53
- Miller R. G., 1977, Journal of the American Statistical Association, 72, 779
- Moran P. A. P., 1973, Sankhyā: The Indian Journal of Statistics, Series A, 35, 329
- Muerset U., Wolff B., Jordan S., 1997, *A&A*, **319**, 201
- Mukhopadhyay S., 2017, Electronic Journal of Statistics, 11, 215
- Mukhopadhyay S., Parzen E., 2014, LP Approach to Statistical Modeling (arXiv:1405.2601)
- Neyman J., 1937, Scandinavian Actuarial Journal., pp 149–199
- Orr A., Molendi S., Fiore F., Grandi P., Parmar A. N., Owens A., 1997, *A&A*, **324**, L77
- Park T., Van Dyk D. A., Siemiginowska A., 2008, The Astrophysical Journal, 688, 807
- Parzen E., 1983, Technical report, Texas A&M University, College Station, Institute of Statistics.
- Parzen E., 2004, Statistical Science, 19, 652
- Pearson K., 1900, The London, Edinburgh, and Dublin Philosophical Magazine and Journal of Science, 50, 157
- Primini F. A., Kashyap V. L., 2014, *ApJ*, **796**, 24
- Reimers D., Cassatella A., 1985, *ApJ*, **297**, 275
- Self S. G., Liang K.-Y., 1987, Journal of the American Statistical Association, 82, 605
- Smirnov N., 1939, Bull. Math. Univ. Moscou, 2, 3
- Smith R. K., 2020, in Society of Photo-Optical Instrumentation Engineers (SPIE) Conference Series. p. 114442C, doi:10.1117/12.2576047
- Smith R. K., Brickhouse N. S., Liedahl D. A., Raymond J. C., 2001, *ApJ*, **556**, L91
- Wilks S. S., 1938, The annals of mathematical statistics, 9, 60
- XRISM Science Team 2022, arXiv e-prints, p. arXiv:2202.05399
- Yamaguchi H., et al., 2008, *PASJ*, **60**, S141
- van Dyk D. A., 2011, in PHYSTAT 2011. CERN, Geneva, pp 148–157, doi:"10.5170/CERN-2011-006.148"

APPENDIX A: PROOF OF THE CONVERGENCE OF K-STATISTIC

Let k_m be the observed value of the K-statistic K_m on the data and $W_j \stackrel{i.i.d}{\sim} \chi_1^2$ for $j = 1, \dots, m$, we have

$$\begin{aligned} P(K_m > k_m | H_0) &= 1 - P(K_m \leq k_m | H_0) \\ &= 1 - P\left(\max_{j=1, \dots, m} n\hat{\theta}_j^2 \leq k_m | H_0\right) \\ &\stackrel{d}{\rightarrow} 1 - P\left(\max_{j=1, \dots, m} W_j \leq k_m\right) \\ &= 1 - P\left(\chi_1^2 \leq k_m\right)^m, \end{aligned}$$

corresponding to Equation (11), where the notation $\stackrel{d}{\rightarrow}$ denotes convergence in distribution, and the convergence is for $n \rightarrow \infty$.

APPENDIX B: PROOF OF THEOREM 1

Consider the event E_m defined as

$$E_m = \left\{ m \text{ maximises the BIC criterion in (12)} \right\}$$

Then, an upper bound for the limit of $P(K_{(m)} \geq k_{(m)} | H_0)$ is

$$\begin{aligned} P(K_{(m)} \geq k_{(m)} | H_0) &= P(K_m > k_m \cap E_m | H_0) \\ &= P\left(\max_{j=1, \dots, m} n\hat{\theta}_{(j)}^2 > k_m \cap E_m | H_0\right) \\ &= P\left(\max_{j=1, \dots, m} n\hat{\theta}_{(j)}^2 > k_m | E_m \cap H_0\right) P(E_m | H_0) \\ &= P\left(\max_{j=1, \dots, M} n\hat{\theta}_{(j)}^2 > k_m | E_m \cap H_0\right) P(E_m | H_0) \\ &\leq \sum_{m=1}^M P\left(\max_{j=1, \dots, M} n\hat{\theta}_{(j)}^2 > k_m | E_m \cap H_0\right) P(E_m | H_0) \\ &= P\left(\max_{j=1, \dots, M} n\hat{\theta}_{(j)}^2 > k_m | H_0\right) \stackrel{d}{\rightarrow} 1 - P\left(\chi_1^2 \leq k_m\right)^M \end{aligned}$$

where the convergence is for $n \rightarrow \infty$, and follows from (11). This proves Theorem 1 (Equation (15)).

APPENDIX C: CORRECTED BACKGROUND DENSITY

The corrected background density for region W_4 (Equation (17)) is calculated as:

$$\begin{aligned} \hat{b}_{W_4}(x) &= \frac{1}{\int_{l_4}^{u_4} \hat{b}_{C_4}(x)} \hat{b}_{C_4}(x) \\ &= \frac{1}{\int_{14.6}^{15.15} (1.3994 - 0.0250x)} (1.3994 - 0.0250x) \\ &= 2.4749 - 0.0441x \end{aligned}$$

where \hat{b}_{C_4} is the corrected background density for the combined region C_4 in (16); l_4, u_4 corresponds to the lower and upper bounds of the wavelength range of region W_4 and $x \in [14.6, 15.15]$ Å. The corrected background density for region W_5 can be derived in a similar manner.

APPENDIX D: ADDITIONAL TABLES

Tables D1 and D2 report the probability of Type I error for our smooth tests and adequate post-selection and multiple hypothesis testing adjustments. Specifically, Table D1 reports the type I errors inclusive only of the post-selection adjustments. Specifically, this corresponds to the probabilities of false discoveries we would expect our testing procedures to have if we were to conduct an analysis on each of the regions considered individually, that is, without simultaneously testing for spectral lines in the remaining six regions. Conversely, in Table D2, we report the probability of a false discovery across the entire spectrum, that is, when accounting for the fact that seven different tests are being conducted simultaneously.

Tables D3 and D4 report the upper limits obtained using smooth tests for the spectral lines of interest. Similarly to the upper limits obtained by means of the LRT, Table D3 and Table D4 provide the local and Sidak adjusted upper limits respectively described in detail in Section 4.3.

Regions of interest (W_r)	Bonferroni	K	Naive	LRT
W_3	0.0511 (± 0.0022)	0.0509 (± 0.0022)	2e-4 ($\pm 1e-4$)	0.0434 (± 0.0020)
W_4	0.0559 (± 0.0023)	0.0500 (± 0.0022)	3e-4 ($\pm 2e-4$)	0.0445 (± 0.0021)
W_5	0.0472 (± 0.0021)	0.0455 (± 0.0021)	3e-4 ($\pm 2e-4$)	0.0422 (± 0.0020)
W_6	0.0511 (± 0.0022)	0.0487 (± 0.0022)	3e-4 ($\pm 2e-4$)	0.0446 (± 0.0021)
W_7	0.0602 (± 0.0024)	0.0497 (± 0.0022)	1e-4 ($\pm 1e-4$)	0.0449 (± 0.0021)
W_8	0.0612 (± 0.0024)	0.0474 (± 0.0021)	3e-4 ($\pm 2e-4$)	0.0471 (± 0.0021)
W_9	0.0619 (± 0.0024)	0.0475 (± 0.0021)	3e-4 ($\pm 2e-4$)	0.0401 (± 0.0020)

Table D1. Simulated type I error and respective Monte Carlo errors for the smooth tests computed on regions W_3 - W_9 and setting the local significance level to 0.05.

Regions of interest (W_r)	Bonferroni	K	Naive	LRT
W_3	0.0118 (± 0.0023)	0.0082 (± 0.0009)	0 (± 0)	0.0070 (± 0.0008)
W_4	0.0130 (± 0.0031)	0.0072 (± 0.0008)	0 (± 0)	0.0057 (± 0.0008)
W_5	0.0102 (± 0.0030)	0.0063 (± 0.0008)	0 (± 0)	0.0063 (± 0.0008)
W_6	0.0114 (± 0.0024)	0.0065 (± 0.0008)	0 (± 0)	0.0058 (± 0.0008)
W_7	0.0133 (± 0.0033)	0.0062 (± 0.0008)	0 (± 0)	0.0060 (± 0.0008)
W_8	0.0139 (± 0.0034)	0.0058 (± 0.0008)	0 (± 0)	0.0070 (± 0.0008)
W_9	0.0142 (± 0.0029)	0.0078 (± 0.0009)	0 (± 0)	0.0056 (± 0.0007)

Table D2. Simulated type I error and respective Monte Carlo errors for the smooth tests computed on regions W_3 - W_9 and adjusted for multiple hypothesis testing using Sidak's correction with global significance $\alpha = 0.05$. In this case, the local significance is $\alpha_r = 1 - (1 - \alpha)^{\frac{1}{R}} = 0.0073$, for $r = 1, \dots, R$.

Local Regions (W_r)	50% Upper limits via smooth tests			90% Upper limits via smooth tests		
	Bonferroni	K	Naive	Bonferroni	K	Naive
W_3	45.26	45.99	61.32	70.08	71.54	85.41
W_4	28.90	31.37	38.53	44.71	48.17	53.60
W_5	35.32	36.74	47.57	55.11	56.99	65.47
W_6	32.76	34.32	44.07	51.09	53.82	60.84
W_7	26.85	30.07	36.70	42.06	45.82	50.12
W_8	26.82	29.87	37.56	41.76	45.53	50.75
W_9	58.50	66.30	79.56	91.65	100.6	110.0

Table D3. 50% and 90% upper limits obtained using smooth tests with different post-selection adjustments. The 50% upper limits are calculated by the proportion of the expected lines η to achieve the power 0.5 (solid line in Figure 4) times the sample sizes n_r . Similarly, the 90% upper limits are calculated by the proportion of the expected lines η to achieve the power 0.9 times the sample sizes n .

Sidak adjusted Regions (W_r)	50% upper limits via smooth tests			90% upper limits via smooth tests		
	Bonferroni	K	Naive	Bonferroni	K	Naive
W_3	53.29	63.88	67.16	77.38	89.06	89.06
W_4	34.09	42.48	42.73	49.40	59.77	57.55
W_5	41.45	50.40	52.28	58.88	69.24	70.18
W_6	39.00	47.19	48.75	56.16	66.69	65.52
W_7	32.76	41.35	41.17	46.54	56.74	53.70
W_8	33.20	39.88	42.20	46.55	54.38	55.68
W_9	71.37	91.26	89.31	101.4	125.2	118.2

Table D4. Sidak's corrected 50% and 90% upper limits obtained using smooth tests with different post-selection adjustments.